

Autonomous Landing of Miniature Aerial Vehicles

D. Blake Barber Stephen R. Griffiths Timothy W. McLain* Randal W. Beard
Brigham Young University Provo, UT 84602

This paper outlines a simple algorithm for automated landing of miniature aerial vehicles (MAVs). Utilizing estimates of height above ground from barometric pressure and optic flow measurements, repeated landings were performed with a 1.5 m wingspan MAV. With height above ground estimated from barometric pressure measurements alone, landing errors averaged 7.6 m. When optic flow and barometric pressure measurements were combined to estimate height above ground, the average landing error was only 4.3 m.

I. Introduction

The usefulness of mini and micro air vehicles (MAVs) depends partly on the ability to hand launch and recover the MAV in uncontrolled environments. Efforts to implement effective autonomous landing of MAVs in uncontrolled environments have been most hindered by lack of small, lightweight, effective sensors to determine height above ground (HAG). Because of the lack of a suitable sensor for determining HAG, MAVs have traditionally relied solely on barometric altimeters for HAG estimation. This approach works well for structured environments in which the altitude of the landing environment relative to the altitude of the takeoff environment is known, and the terrain is relatively smooth. However, in uncontrolled environments where this offset is not known, or where the terrain is not acceptably smooth, other methods must be utilized to effectively determine HAG.

One method for that has been recently proposed for HAG estimation combines measurements of optical flow and ground speed. By correlating the optic flow of the ground observed from the MAV with the ground speed determined from GPS measurements, an estimate of the height of the MAV above the ground can be made. Estimates of HAG from optic flow can be combined with information from the barometric altimeter to determine HAG over a large altitude range. This estimate of HAG can then be combined with landing control algorithms to safely land MAVs. This paper presents the experimental results of efforts to estimate HAG and land small fixed-wing MAVs in uncontrolled environments using an optic flow sensor.

Most of the work done regarding autonomous landing of small unmanned aerial vehicles (UAVs) has focused on the autonomous landing of unmanned rotary aircraft. Most of these approaches involve using image processing techniques to estimate the pose of the UAV based on the motion of the aircraft relative to a structured target.^{1,2} Researchers at the Army/NASA Rotorcraft Division have developed a method for landing an unmanned rotorcraft based on vision processing techniques, that does not require a structured reference image or structured landing environment.^{3,4}

These techniques, though effective for rotary aircraft, do not work well for fixed-wing MAVs. Development of robust landing algorithms for fixed-wing MAVs has been most hindered by the lack of a sensor with acceptably small payload and acceptably high reliability for estimating height above ground (HAG). Recently, much of the research in this area has focused on utilizing vision processing techniques to estimate HAG. Chahl, et al.⁵ demonstrated that mimicking the landing behavior of bees, by maintaining constant optic flow during a landing maneuver, could be used to successfully control the descent of a MAV. Development of lightweight sensors for measurement of optic flow⁶⁻⁸ has further bolstered the optic flow based approach. Barrows, et al. have demonstrated that these sensors can be successfully used to follow terrain in low flying MAVs.⁹

The use of optic flow data for flight control is a subject of ongoing research. This is especially true regarding the use of optic flow data in autonomous landing of MAVs. Quigley, et al. presented an algorithm

*Corresponding author, email: mclain@byu.edu

for the autonomous landing of MAVs utilizing barometric pressure sensing.¹⁰ Algorithms for augmenting this pressure-based method with data from optic flow are presented in this paper.

The landing algorithm utilized in this research is presented in section II. The longitudinal and lateral-directional control laws used for automated landing are described in section III. Pressure-based HAG estimation and optic flow-based HAG estimation are discussed in section IV. Section V presents the flight test hardware used, while section VI presents automated landing results for MAVs using pressure-based and optic flow-based HAG estimation.

II. Landing Algorithm Overview

The landing algorithm developed and tested for this project consists of two user defined waypoints: the approach point and the landing point (Figure 1). The MAV orbits around the approach point as it descends to a specified altitude. At this end altitude, it breaks out of its orbit and follows a glide slope to the landing point. The approach point is fully defined by the following parameters:

1. Airspeed - The airspeed during the spiral-down portion of the landing.
2. Radius - The radius of the orbit during the spiral-down portion of the landing
3. Start Altitude - The altitude to which the plane climbs or descends while en route to the approach point. The true start altitude for the descent will be the altitude to which the plane has successfully climbed or descended by the time it is within 1.5 orbit radii of the landing point.
4. End Altitude - The altitude at which the airplane breaks out of its orbit and begin its glide slope to the landing point
5. Relative East Coordinate - The distance east of home (in meters) around which the plane orbits while descending from its start altitude to its end altitude.
6. Relative North Coordinate - The distance north of home (in meters) around which the plane orbits while descending from its start altitude to its end altitude.
7. Descent Rate - The rate (in meters/second) at which the plane descends while orbiting the approach point.

The landing point is fully defined by the following parameters:

1. Airspeed - The airspeed during the glide slope from approach point to landing point.
2. Flare Height - The height above ground at which the airplane cuts the throttle and attempts to hold zero roll while maintaining its glide slope by commanding pitch to control around desired altitude.
3. Relative East Coordinate - The distance east of home (in meters) at which the plane will touch down.
4. Relative North Coordinate - The distance north of home (in meters) at which the plane will touch down.

III. Control Approach

A. Altitude Control

Altitude control throughout the landing routine is accomplished through activation of several PID loops. For the portion of the landing sequence during which the plane is en route from its last waypoint to the approach point altitude is maintained according to the following criteria:

1. If the actual altitude is within a preset distance (usually around 15 m) of the desired altitude, then Pitch from Altitude and Throttle from Airspeed control laws are used.
2. If the actual altitude is greater than the preset distance from the desired altitude and is less than the desired altitude, then the Pitch from Airspeed control law is used with full throttle.

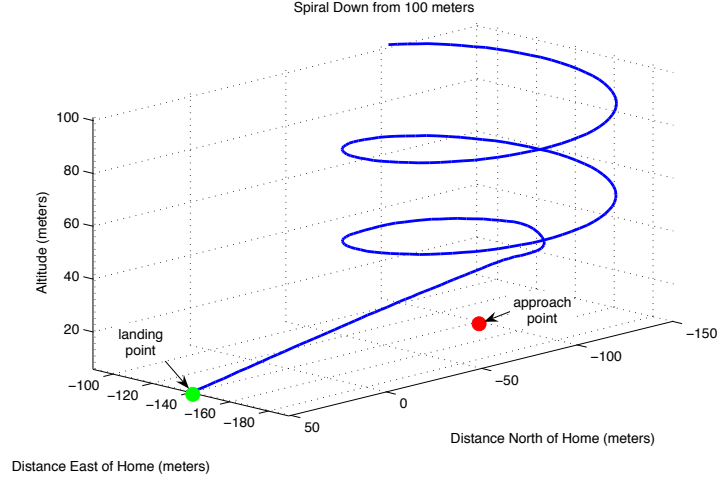


Figure 1. Landing spiral approach point and landing point.

3. If the actual altitude is greater than the preset distance from the desired altitude and is greater than the desired altitude, then the Pitch from Airspeed control law is used with zero throttle.

For the portion of the landing sequence in which the plane is spiraling down to its end altitude and then following its glide slope to the landing point, altitude is maintained using the pitch from altitude and throttle from airspeed loops. Throughout the entire landing sequence, until the flare at which desired roll is held at zero, heading is controlled using the Roll from Heading PID loop. Roll rate and pitch rate are also controlled to provide damping. Desired headings are commanded based on the generation of a heading field which forms a limit cycle around the desired orbit radius. A full description of this algorithm is provided in the following section.

1. *Glide Slope*

The glide slope implemented in this landing routine was a simple linear glide slope calculated by decreasing desired altitude as a function of the distance from where the glide slope began. This formulation allows the desired altitude to be driven negative for distances from the initiation of the glide slope that are farther than the desired landing point. This makes the glide slope robust with respect to negative offsets between measured HAG and actual HAG. Expected overshoot or undershoot of the landing point can approximated as

$$\text{Expected Over / Undershoot} \approx \frac{1}{\tan \theta} (\tilde{h} + u_h), \quad (1)$$

where θ is the glide slope, \tilde{h} is the altitude control error (difference between desired and actual HAG), and u_h is the measurement error. The relationship shown in Equation (1) indicates that larger glide slopes will tend to reduce the overall overshoot or undershoot error for the landing provided the plane is capable of matching the commanded glide slope. However, larger glide slopes also cause increased impact velocities at touch down. Testing showed that glide slopes between 7 to 12 degrees provided a good balance between accuracy and impact at touch down for the MAVs flown.

B. Orbit Routine

1. *Heading Vector Field Generation*

The ability to implement the landing routine described in Section II required the development and implementation of a control algorithm that would allow the airplane to fly accurate orbits, at minimal orbit radii, even in high wind conditions. The orbit algorithm implemented generates a desired ground track heading

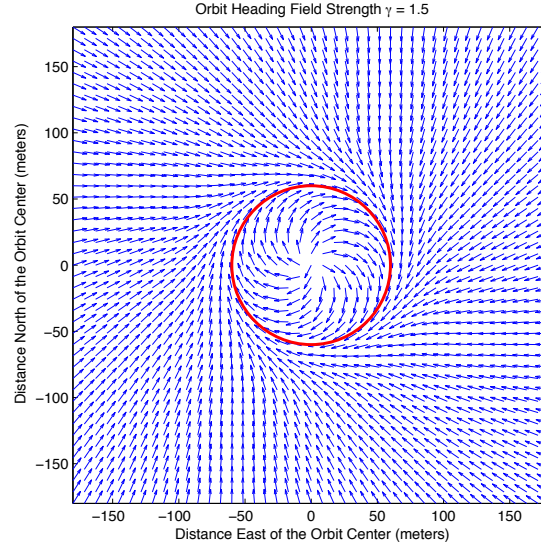


Figure 2. Heading field for a 50 m radius orbit.

(χ_d) based on the position of the airplane so that the resulting heading vector field directs the MAV onto the desired orbit (Figure 2). Such a heading field is generated using Equation (2).

$$\chi_d = \begin{cases} \chi_c - \tan^{-1} \left(\frac{r_c}{d} \right), & d \geq 2r_c \\ \chi_c - \alpha - \beta \bar{r}^\gamma, & r_c \leq d \leq 2r_c \\ \chi_c + \alpha + \pi + \beta \bar{r}^\gamma, & d < r_c \end{cases} \quad (2)$$

In the above equations d is the distance from the center of the orbit, χ_d is the desired course, χ_c is the compass heading to the center of the orbit, r_c is the desired orbit radius, α is the included angle between χ_d and χ_c for $d = 2r_c$, β is the complimentary angle to α , and γ is a gain corresponding to the field strength of the orbit. Increasing γ makes the field more strongly attracted to the desired orbit radius and decreasing γ makes the field less attracted as shown in Figures 3 and 4. \bar{r} is a parameterization of the distance from the center of the orbit based on r_c . The formulation of \bar{r} is such that $0 \leq \bar{r} \leq 1$, and $\bar{r} = 1$ when $d = r_c$. The value of \bar{r} is calculated according to Equations (3).

$$\bar{r} = \begin{cases} 1 - \frac{d-r_c}{r_c}, & r_c \leq d \leq 2r_c \\ \frac{d}{r_c}, & d < r_c \end{cases} \quad (3)$$

The desired heading from the heading field described by Equation (2) is used to generate a roll command for the airplane according to

$$\phi_d = k(\chi_d - \chi), \quad (4)$$

where χ is the ground track heading determined from GPS measurements.

2. Steady State Error Correction

Because the heading control system is type I and an orbit is a ramp in heading, the heading of the airplane tracks the desired heading with a constant steady-state error. This steady-state error in heading represents a lag between desired and actual heading which translates to orbits that are larger than the commanded orbit. The magnitude of the steady-state error in orbit radius is a function of the desired radius of the orbit, the groundspeed of the airplane, and the heading field gain γ . Two different approaches were used to reduce this error. The first approach involved adapting the radius command to remove the steady-state error. The second approach, which was more effective in high winds, involved calculating a nominal roll angle based on

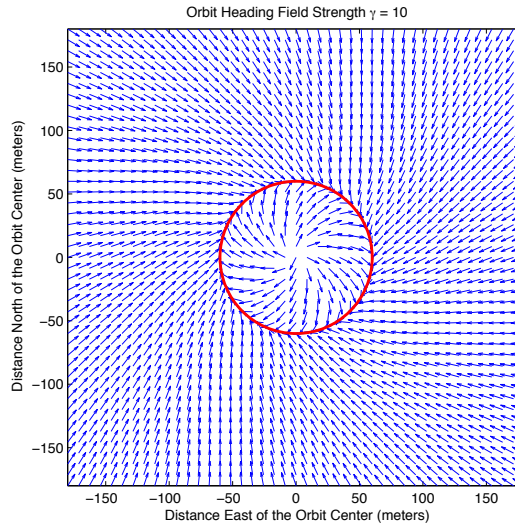


Figure 3. High gain heading field for a 50 m radius orbit.

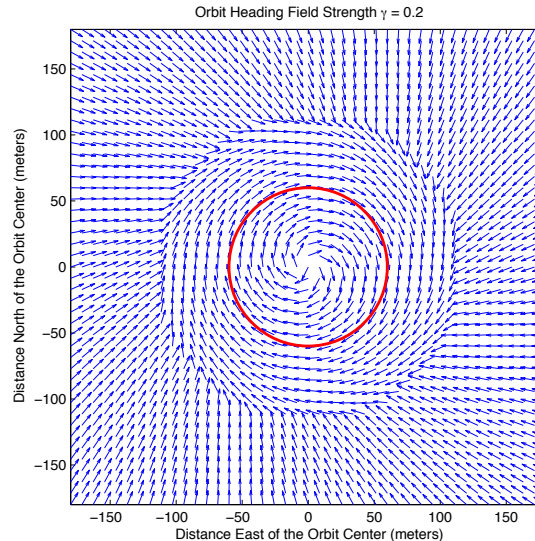


Figure 4. Low gain heading field for a 50 m radius orbit.

the desired heading rate and the coordinated turn equation and adding that into the control as a feedforward command.

ADAPTIVE RADIUS COMMANDS Because the actual orbit radius of the airplane is always larger than the commanded radius, for every dynamically feasible orbit there exists some smaller radius command that will result in the desired orbit. The adaptive radius command progressively increases or decreases an offset between the desired orbit radius entered by the operator and the desired orbit radius passed to the orbit algorithm. This offset is continuously incremented or decremented until the plane is orbiting at the radius requested by the operator. Orbit results from flight tests of the adaptive radius method are shown in Figure 5.

FEEDFORWARD ROLL ANGLE BASED ON DESIRED HEADING RATE The adaptive radius command approach works extremely well for situations where wind speed does not exceed 50 percent of airspeed. However, high winds cause the groundspeed of the airplane to vary significantly based on the course of the

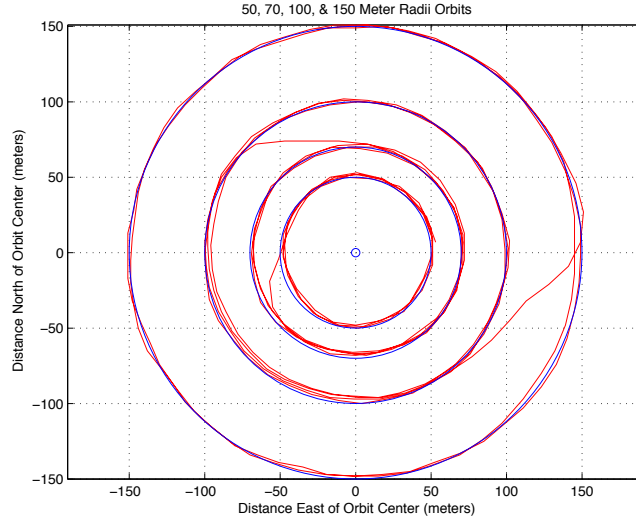


Figure 5. Flight test results for 50, 70, 100, and 150 m orbits flown in 2 to 3 m/s wind.

airplane relative to the wind direction. This variation in groundspeed causes a corresponding variation in the radius offset necessary to maintain the desired orbit. A better approach for high wind conditions was developed that involved calculating a nominal feedforward roll angle command corresponding to the heading rate required to fly the desired orbit. The feedforward roll command was used to augment the feedback command generated from the heading error. Calculating the feedforward roll command required taking the derivative of the heading field with respect to time. Heading rate is given by

$$\dot{\chi}_d = \begin{cases} \frac{V r_c (r_c^2 + 2d^2)}{d(r_c^2 + d^2)^{\frac{3}{2}}}, & d \geq 2r_c \\ \frac{V}{d} \sin(\alpha + \beta \bar{r}^\gamma) + \bar{r}^{(\gamma-1)} \left(\frac{\gamma \beta V \cos(\alpha + \beta \bar{r}^\gamma)}{r_c} \right), & r_c \leq d \leq 2r_c \\ \frac{V}{d} (\sin(\alpha + \beta \bar{r}^\gamma) - \bar{r}^\gamma \gamma \beta \cos(\alpha + \beta \bar{r}^\gamma)), & d < r_c \end{cases} \quad (5)$$

Equation (2) and Equation (5) allow the calculation of both a desired heading and a desired heading rate for any location relative to the center of the orbit. The desired heading rate can then be converted to a nominal roll angle using the standard coordinated turn equation

$$\phi_{\text{nom}} = \frac{\dot{\chi}_d V}{g} \quad (6)$$

and the control law described in Equation (4) can be adapted as

$$\phi_d = \phi_{\text{nom}} + k(\chi_d - \chi) \quad (7)$$

The control law shown in Equation (7) is more effective than the adaptive radius command method at tracking orbits in high winds, but somewhat less steady at tracking orbits in low wind conditions.

IV. Height Above Ground Estimation

A. Barometric Altimeter Based Landing

The autopilot hardware used comes equipped with a barometric pressure sensor as part of its standard sensor suite. Before a given flight, the barometric pressure sensor is zeroed so that it references the barometric pressure at the takeoff location as the pressure corresponding to zero altitude. Pressure decreases with altitude according to

$$P = P_{\text{ref}} - \int_{h_{\text{ref}}}^h \rho g h \, dh. \quad (8)$$

If the density of air (ρ) is assumed to be constant over the range of altitudes being measured, then altitude above the takeoff point can be determined by

$$h = \frac{P_{\text{ref}} - P_{\text{actual}}}{\rho g} = \alpha (P_{\text{ref}} - P_{\text{actual}}), \quad (9)$$

where the constant of proportionality (α) can be determined by calibration. Once the constant of proportionality has been determined, readings of the pressure sensor from the analog to digital converter can be converted directly into relative altitudes above the takeoff point. This calibration allows the barometric pressure sensor to provide valid and accurate estimates of HAG where the terrain is flat. Where this is not true, barometric pressure can still provide a rough estimate of HAG until other sensors are able to collect more precise readings of the true HAG.

B. Optic Flow Based Landing

Optic flow sensors can be used to determine HAG by relating the flow of features across an imaging array to the speed the imaging array is moving past the surface it is imaging and its distance from that surface. The number of pixels that a given object moves in the imaging plane can be combined with data from the MAVs IMU and GPS to determine HAG⁷ according to

$$h = \frac{\delta x}{2 \tan \left(\frac{\gamma^{\text{fov}}}{2p_n} - \frac{\dot{\theta} T_s}{2} \right)} \cos \theta \cos \phi, \quad (10)$$

where h represents HAG, δx represents the displacement of the sensor parallel to the plane being imaged over the sample period T_s , γ represents the average number of pixels of displacement of features across the imaging plane over the same sample time, fov represents the field of view of the sensor, p_n is the number of pixels in the imaging array in the direction of motion of the sensor, $\dot{\theta}$ is the average pitch rate of the sensor over the sample period, θ is the average pitch of the sensor over the sample period, and ϕ is the average roll of the sensor over the sample period.

SENSOR Testing of autonomous landing using optic flow to determine HAG was performed using Agilent's ADNS-2610 optic flow sensor. The ADNS-2610 has a small form factor, measuring only 10 mm by 12.5 mm and runs at 1500 frames per second. It requires a light intensity of at least 80 mW/m² at a wavelength of 639 nm or 100 mW/m² at a wavelength of 875 nm. The ADNS-2610 measures the flow of features across an 18 by 18 pixel CMOS imager. It outputs two values, dx and dy , representing the total optic flow across the sensor's field of view in both the x and y directions. These values are stored in a buffer which can store accumulated optic flow up to 128 pixels. Once the buffer is full no more optic flow readings are accumulated until the buffer has been read. Reading the buffer clears it and allows it to begin reaccumulating optic flow measurements. The flow data in the camera y direction corresponds to lateral motion of the airplane, and for purposes of estimating HAG can be ignored. The flow data in the camera x direction can be combined with data from the IMU and GPS to determine HAG according to Equation (10).

OPTICS A critical consideration in outfitting an airplane with an optic flow sensor is the setup of the optics. Narrow angle lenses increase the distance at which the airplane will be able to pick up appreciable optic flow. This increases the distance at which the sensor will be able to accurately measure HAG for a given groundspeed. This comes at the expense of increasing the longitudinal size of the sensor. Narrow angle lenses can also decrease the low end range of the sensor by causing overflow in the optic flow sensor's dx register or by causing the flow rate seen by the sensor to become too fast for the sensor to register. Wide angle lenses allow for smaller longitudinal sensor size, but require that larger features be available in the environment. They also decrease the distance at which appreciable optic flow will be recorded for a given groundspeed. A particular advantage of wider angle lenses is that they are less susceptible to noise introduced by angular oscillations of the airplane in pitch and roll.

In addition to focal length, lens diameter is an important consideration. This is especially important with regard to the corresponding f-stop value of the lens. The f-stop is defined as the ratio of a lens' focal length to its diameter and is a measure of the amount of light that the optics allow to pass through to the imaging array. Lenses with larger f-stops allow less light to pass through. Keeping in mind that the imaging array requires a light intensity of 80 to 100 W/m² in the correct spectral range, it is important to select a

lens with a low f-stop in order to increase the sensor's operational range. Because the sensor automatically adjusts shutter speed to keep the light intensity at an ideal level, there is no disadvantage to selecting a lens with a lower f-stop other than increased size. Another important implication of the f-stop is that selecting a lens with an increased focal length (a narrower angle lens) will not only increase the length of the sensor, but also increase the diameter of the sensor if the f-stop is to be maintained.

For the purposes of these tests lenses were selected which yielded fields of view of 6.5, 2.5, and 1.2 degrees when mounted on the sensor. These lenses had accompanying f-stops of 2.0, 2.0, and 2.5 respectively. Each of the configurations is shown in Figure 6. Comparable results were achieved using both the 2.5 degree and 1.2 degree field-of-view setups. However, the 1.2 degree field-of-view lens offered the slightly greater range while performing better over feature poor surfaces such as asphalt. The one disadvantage of the 1.2 degree field of view setup up was its increased susceptibility to noise caused by pitch and roll oscillations.



Figure 6. 1.2, 2.5, and 6.5 degree field of view optics configurations.

SAMPLE RATE Another critical consideration when equipping an airplane with an optic flow sensor is the selection of sample rate. The resolution of the sensor (measured in units of distance per sensor count) is given by

$$r = \lim_{\delta_h \rightarrow 0} \left(\frac{\delta_h \frac{\text{fov}}{2p_n}}{\tan^{-1} \left(\frac{Vt_s}{2(h-\delta_h)} \right) - \tan^{-1} \left(\frac{Vt_s}{2h} \right)} \right) \quad (11)$$

where V is groundspeed and δ_h is a perturbation to the HAG. For a given sensor with a fixed field of view, the sensor's resolution is a function of sample rate, groundspeed, and HAG. Plots of sensor resolution for a fixed field of view and varying sample rates and groundspeeds are shown in Figures 7 and 8.

For high values of r , each sensor count corresponds to a relatively large distance measure. Correspondingly the noise on the sensor measured in sensor counts is amplified by r into higher magnitude noise in the HAG measurement. This makes large values r undesirable because they can significantly decrease the sensor's signal to noise ratio. It is possible to decrease r by decreasing the sample rate as shown in Figure 7. This, however, can be undesirable because it decreases the sensor's response time and can lead to overflow in the sensor's dx register. Furthermore, for a fixed sample rate, maintaining a low value of r for large values of HAG results in unnecessarily low values of r for lower values of HAG. This means unnecessarily low sample rates are being maintained where significantly faster sample rates could be used without significant loss in signal to noise ratio. Such an approach also results in premature sensor overflow and corresponding loss of low-end range. To solve these problems two approaches were developed using a dynamic rather than static sample rate. The first approach maintains an r value along a specified resolution curve regardless of groundspeed of the plane. The second approach uses the current velocity estimate and HAG estimate to maintain a constant value of r regardless of groundspeed and HAG.

CONSTANT CURVE RESOLUTION In general, flight control systems for UAVs utilize a feedback loop to control around a commanded airspeed rather than groundspeed. Even when the feedback loop is closed

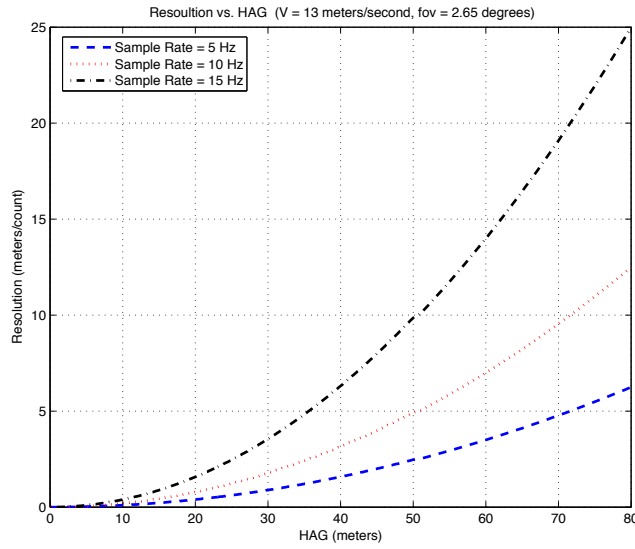


Figure 7. Resolution as a function of HAG and sample rate.

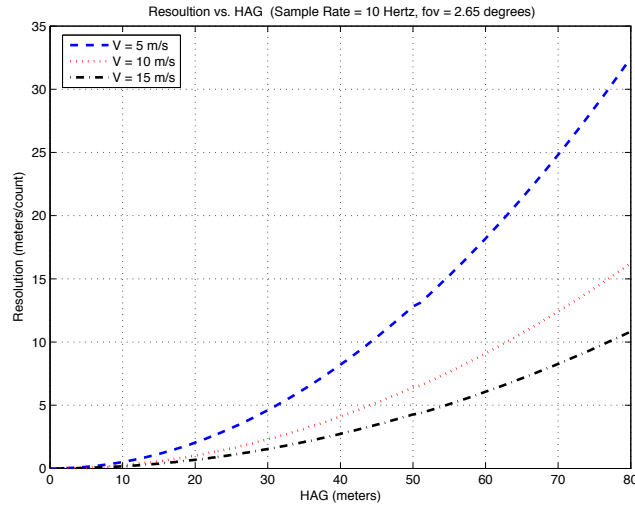


Figure 8. Resolution as a function of HAG and groundspeed.

around groundspeed, the commanded groundspeed may not be realizable due to wind conditions. In the presence of wind it is reasonable to assume that groundspeed may vary significantly depending on the course of the airplane relative to the wind direction. As shown in Figure 8 variations in groundspeed can alter the resolution curve significantly. However, if the sample period is set according to

$$T_s = \frac{\tau}{V}, \quad (12)$$

where τ represents the sample rate divisor, the value of r will follow a fixed resolution curve as a univariate function of HAG, such as those shown in Figures 7 and 8. This is useful because it eliminates the variations in resolution due to velocity and provides reliable repeatable resolutions regardless of wind conditions or commanded airspeeds.

CONSTANT VALUE RESOLUTION When an estimate of the current HAG is available, the correct sample rate can be calculated such that the sensor resolution can be maintained constant regardless of HAG or groundspeed. This sample period is found by solving Equation (11) for T_s . The result is

$$T_s = \lim_{\delta_h \rightarrow 0} \left(\frac{1}{\left(\frac{V}{2(h-\delta_h)} - \frac{V}{2h} \right) \frac{1}{\tan\left(\frac{\delta_h \text{fov}}{2p_n r}\right)} - \frac{V^2}{4h(h-\delta_h)}} \right), \quad (13)$$

where r now represents a user defined parameter that defines the resolution of the sensor for all combinations of HAG and groundspeed. In practice, the actual value of T_s is capped at both the high and low end, but allowed to vary over a given range to maintain a fixed resolution. In flight tests using a dynamic sample rate to fix sensor resolution cut noise drastically for high values of HAG while significantly increasing the sample rate and thus improving the response time for low values of HAG. In practice Equation (13) is implemented by dropping the limit expression and setting δ_h to zero.

Flight test results using both constant curve resolution and constant value resolution are shown in Figures 9 and 10. The spikes in the optic flow measurement at sample 275 in the constant curve resolution plot and 400 in the constant value resolution plot correspond to flight over an asphalt road. In practice such spikes are ignored by discarding measurements for which the optic flow sensors report poor surface quality.

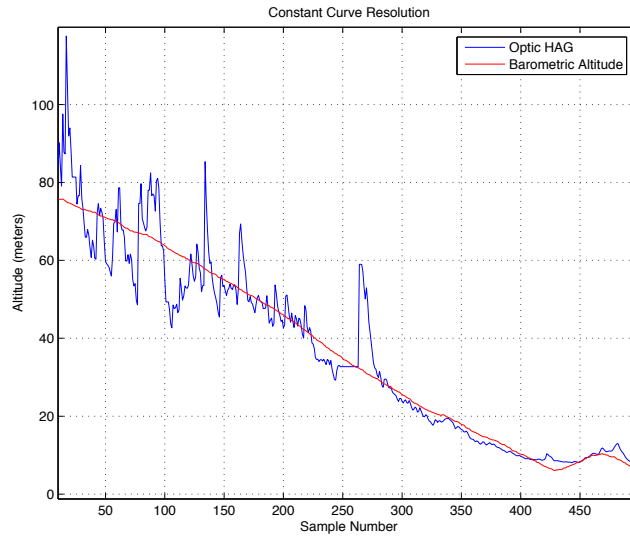


Figure 9. Optic HAG results from glideslope descents using fixed-curve resolution.

The accuracy of the distance measurements calculated from optic flow was tested by comparison with a laser rangefinder. Testing was performed by mounting the optic flow sensor and laser rangefinder perpendicular to the motion of a vehicle driving along a freeway at varying distances from the freeway sound barrier wall. Range values were recorded for both the optic flow calculations and the laser rangefinder. The results of this test are shown in Figure 11. The results show close agreement and validate the readings obtained from the optic flow calculations.

Range data from the optic flow sensor in flight tests showed reliable, repeatable readings for heights above ground less than 40 m. For the purposes of landing based on HAG calculations from optic flow, values above 40 m were discarded as noise.

V. Flight Test Hardware

BYU has developed a reliable and robust platform for unmanned aerial vehicle testing. Figure 12 shows the key elements of the testbed. The first frame in Figure 12 shows the ground station components. A laptop runs the Virtual Cockpit software that interfaces through a communication box to the MAVs. An

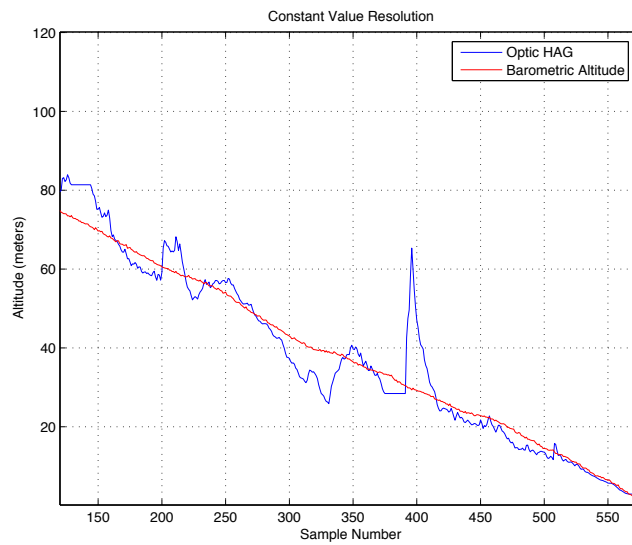


Figure 10. Optic HAG results from glideslope descents using fixed-value resolution.

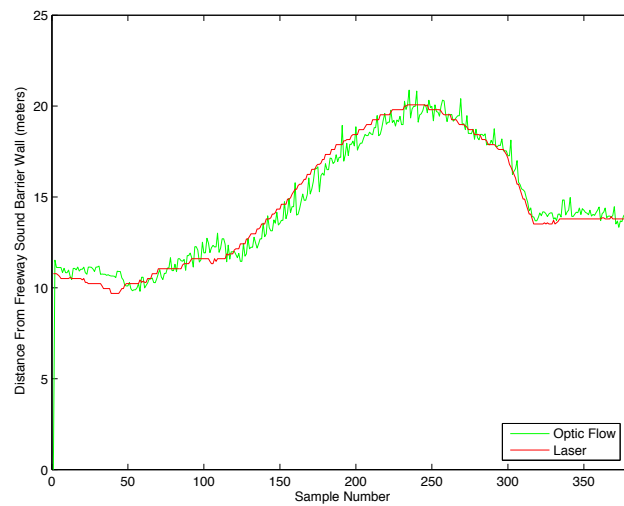


Figure 11. Optic flow range data compared to laser rangefinder data.



Figure 12. (a) Ground station components (b) Kevlar covered flying wing airframe (c) Kestrel autopilot

RC transmitter is used as a stand-by fail-safe mechanism to facilitate safe operations. The second frame in Figure 12 shows the airframe used for the flight tests reported in this paper. The airframe has a 1.5 m wingspan and was constructed with an EPP foam core covered with Kevlar. This design was selected for its durability, useable payload, ease of component installation, and flight characteristics. The airframe can carry a 12 ounce payload and can remain in flight for over 30 minutes at a time. Embedded in the airframe are the Kestrel autopilot, batteries, a 1000 mW, 900 MHz radio modem, a 12 channel GPS receiver, a video transmitter, a 400 m laser rangefinder, a small analog video camera, and three optic flow sensors. The third frame shows BYU's Kestrel autopilot which is equipped with a Rabbit 3400 29 MHz processor, rate gyros, accelerometers, absolute and differential pressure sensors. The autopilot measures $3.8 \times 5.1 \times 1.9$ cm and weighs 18 grams. The autopilot also serves as a data acquisition device and is able to log 175 kbytes of user-selectable telemetry at rates up to 60 Hz.

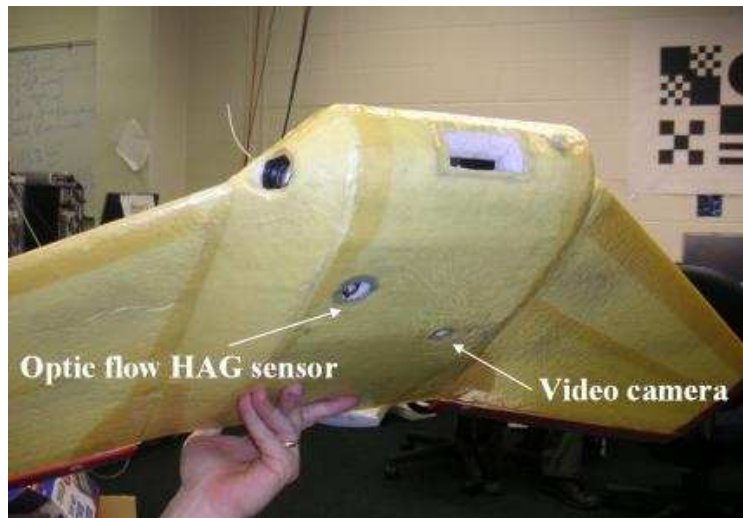


Figure 13. Optic HAG sensor and a downward pointed video camera on underside of airframe.

VI. Autonomous Landing Results and Discussion

A. Pressure Based HAG

Using the calibration described above and testing over relatively short flights, the MAGICC Lab airplanes consistently read within 1 to 1.5 m of the actual altitude relative to home. This allows relatively accurate landings where the altitude of the landing point can be safely assumed to be the same as the altitude of home. This works especially well when trying to land the airplane at or near its home location.

If the actual altitude of the airplane matched the desired altitude perfectly, then overshoot or undershoot would be solely a function of error in HAG estimation. For glide slopes of 7 to 12 degrees and a measurement error of 1 to 1.5 m, a corresponding overshoot or undershoot error of around 4 to 12 m can be expected (see Equation (1)).

Actual results for 26 consecutive landing runs are shown below in Figure 14. The first 22 autoland runs were each from the main approach point. These were followed by one run apiece from each of the four alternate approach points. An average overshoot or undershoot error of 4 to 12 m was estimated. Actual results from these 26 landing show an average over/undershoot error of 7.6 m with a standard deviation of 5.4 m and a median value of 6.0 m.

B. Optical Flow Based HAG

Using the fixed value resolution sample rate and the 2.65 degree field of view optics, HAG measurements based on optic flow were used to perform twenty-seven consecutive autonomous landings from a single approach point. The results are shown in Figure 15. For each of these autonomous landings HAG was calculated

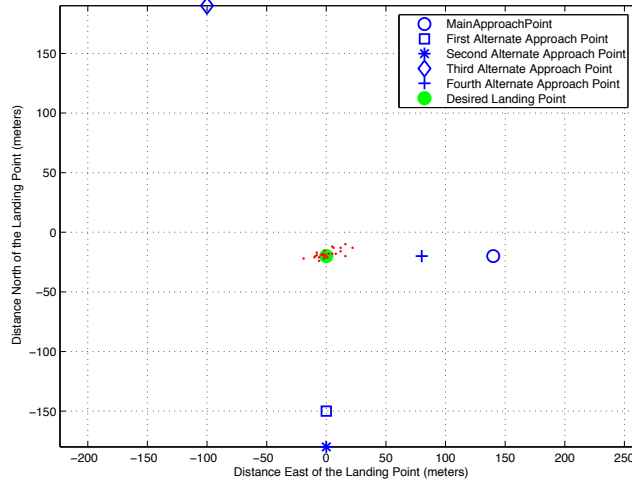


Figure 14. Pressure-based HAG autonomous landings.

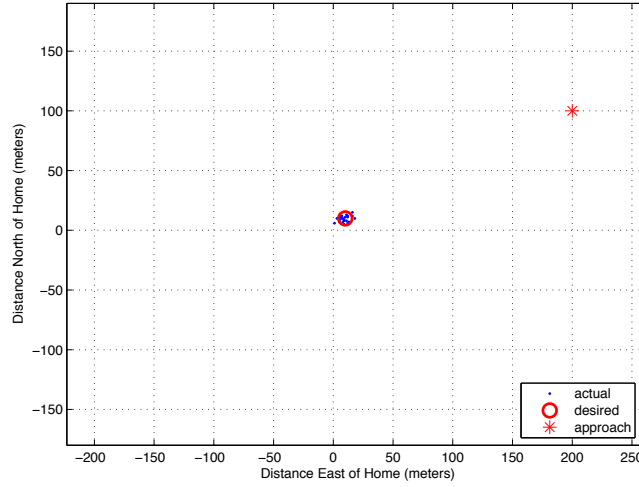


Figure 15. Optic flow-based HAG autonomous landings.

according to

$$h = h_{\text{bar}} + h_{\text{offset}} \quad (14)$$

$$h_{\text{offset}} = \alpha (h_{\text{bar}} - h_{\text{optic}}) + (1 - \alpha) h_{\text{offset}}. \quad (15)$$

The value of h was updated every time through the loop and the value of h_{offset} was updated every t_s seconds where t_s varied with the current HAG estimate and groundspeed.

The readings from the barometric pressure sensor were allowed to drift over the twenty-seven landings in order to simulate an unknown landing point altitude. The barometric altimeter drifted to 15 m of inaccuracy over the first 22 landings and was then rezeroed to introduce negative offsets between true HAG and barometric altitude. The value of h_{offset} (corresponding to the drift in the barometric altimeter) for each of the landings is shown in the lower plot of Figure 16. The second subplot of Figure 16 shows the distance from the landing point for each of the 27 landings.

The average distance between the desired and actual touchdown points for autonomous landings using optic flow data was 4.3 m. This represents a 56 percent improvement over the average distance from the

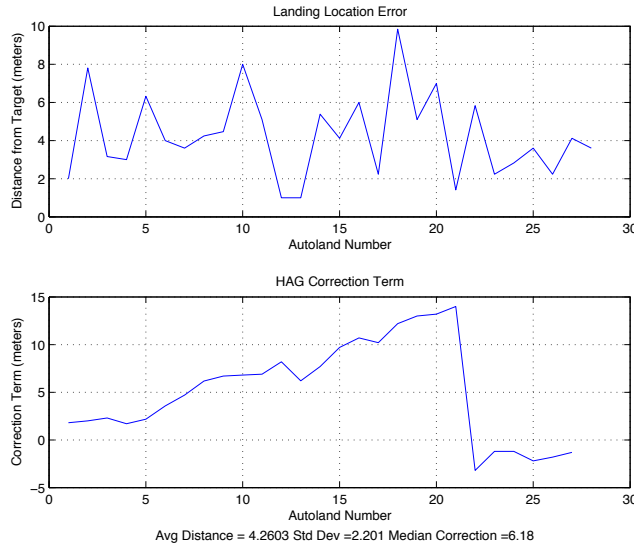


Figure 16. Landing error and HAG correction.

desired touchdown point using only the barometric altimeter. Landings based on HAG from optic flow also had a much narrower spread than those based on barometric altitude alone with a standard deviation of 2.2 m for optic flow based landings compared to 5.4 m for barometric.

Because the circle down portion of the landing routine is based on barometric altitude until HAG readings fall under the 40 m threshold, it is important to note that the distance from the desired touchdown point does not increase with increasing error in barometric altitude. This demonstrates the ability of the optic flow sensor to land the airplane accurately even when the altitude of the landing point relative to the takeoff point is not known.

VII. Conclusions

A simple algorithm for performing autonomous MAV landings has been presented. This landing algorithm utilizes a lateral-directional control method based on heading fields. This algorithm has been tested both in simulation and in hardware and has proven effective, repeatable, and robust to wind. The algorithm has been used effectively to perform hundreds of autonomous landings in a wide variety of wind conditions.

This paper demonstrates that the precision of autonomous landing can be enhanced by direct measurement of height above ground. In environments where the terrain is flat and the altitude of the landing point relative to the takeoff point is known, a well-calibrated barometric altimeter is sufficient to accurately determine HAG. In environments where this is not the case, fusion of data from the barometric altimeter and the optic flow sensor provides a feasible and robust method for estimating HAG. When utilized by the landing algorithms presented in this paper, automated landings to within several meters can be performed repeatably.

VIII. Acknowledgments

Acknowledgments

This work was funded by AFRL/MNK award number F08630-03-1-0017.

References

¹Shakernia, O., Vidal, R., Sharp, C. S., Ma, Y., and Sastry, S., "Multiple View Motion Estimation and Control for Landing an Unmanned Aerial Vehicle," *Proceedings of the 2002 IEEE International Conference on Robotics & Automation*, Washington

DC, May 2002, pp. 2793–2798.

²Sharp, C. S., Shakernia, O., and Sastry, S. S., “A Vision System for Landing an Unmanned Air Vehicle,” *Proceedings of the 2001 IEEE International Conference on Robotics & Automation*, Seoul, May 2001, pp. 1720–1727.

³Hintze, J., Christian, D., Theodore, C., Tischler, M., and McLain, T., “Automated Landing of a Rotorcraft UAV in a Non-cooperative Environment,” *Proceedings of the 60th Annual Forum of the American Helicopter Society*, Baltimore, Maryland, June 2004.

⁴Theodore, C., Sheldon, S., Rowley, D., McLain, T., Dai, W., and Takahashi, M., “Full Mission Simulation of a Rotorcraft Unmanned Aerial Vehicle for Landing in a Non-Cooperative Environment,” *Proceedings of the 61st Annual Forum of the American Helicopter Society*, Grapevine, Texas, June 2005.

⁵Chahl, J., Srinivasan, M., and Zhang, S., “Landing Strategies in Honeybees and Applications to Uninhabited Airborne Vehicles,” *The International Journal of Robotics Research*, Vol. 23, No. 2, 2004, pp. 101–110.

⁶Barrows, G. and Neely, C., “Mixed-mode VLSI optic flow sensors for in-flight control of a micro air vehicle,” *Proceedings SPIE*, San Diego, August 2000, pp. 52–63.

⁷Ruffier, F. and Franceschini, N., “Visually Guided Micro-Aerial Vehicle: automatic take off, terrain following, landing and wind reaction,” *Proceedings of the 2004 IEEE International Conference on Robotics & Automation*, New Orleans, 2004, pp. 2339–2346.

⁸Zufferey, J.-C. and Floreano, D., “Toward 30-gram autonomous indoor aircraft: Vision-based obstacle avoidance and altitude control,” *Proceedings of the 2005 IEEE International Conference on Robotics & Automation*, Barcelona, April 2005.

⁹Barrows, G. L., Chahl, J. S., and Srinivasan, M. V., “Biomimetic Visual Sensing and Flight Control,” *The Aeronautical Journal, London: The Royal Aeronautical Society*, Vol. 107, 2003, pp. 159–168.

¹⁰Quigley, M., Barber, D. B., Griffiths, S., and Goodrich, M. A., “Towards Real-World Searching with Fixed-Wing Mini-UAVs,” *Proceedings of the 2005 IEEE/RSJ International Conference on Intelligent Robots and Systems*, Edmonton, Alberta, August 2005.